References

[1]Rumelhart, D. E., Hinton, G. E., and Williams, R. J., "Learning Internal Representations by Error Propagation," *Parallel Distributed Processing: Explorations in the Microstructure of Cognition Volume 1: Foundations*, Massachusetts Inst. of Technology Press, Cambridge, MA, 1986, pp. 318–364.

[2]Hartman, E., and Keeler, J. D., "Semi-Local Units for Prediction," *IJCNN-91-Seattle: International Joint Conference on Neural Networks*, Vol. II, IEEE, Piscataway, NJ, 1991, pp. 561–566.

[3]Hartman, E., and Keeler, J. D., "Predicting the Future: Advantages of Semilocal Units," *Neural Computation*, Vol. 3, No. 4, 1991, pp. 566–578.

[4]Widrow, B., and Hoff, M. E., "Adaptive Switching Circuits," *1960 WESCON Convention*, Inst. of Radio Engineers, New York, 1960, pp. 96–104.

Numerical Analysis of Base Flowfield for a Four-Engine Clustered Nozzle Configuration

Ten-See Wang*
NASA Marshall Space Flight Center, Huntsville, Alabama 35812

Introduction

EXCESSIVE base heating has been a problem for many launch vehicles. For certain designs such as the direct dump of turbine exhaust inside and at the lip of the nozzle, the potential burning of the turbine exhaust in the base region can be of great concern. Accurate prediction of the base environment at altitudes is therefore very important during the vehicle design phase. Otherwise, undesirable consequences may occur.

In this study, the turbulent base flowfield of a cold flow experimental investigation[1] for a four-engine clustered nozzle was numerically benchmarked using a pressure-based computational fluid dynamics (CFD) method. This is a necessary step before the benchmarking of hot flow and combustion flow tests can be considered. Since the medium was unheated air, reasonable prediction of the base pressure distribution at high altitude was the main goal. Several physical phenomena pertaining to the multiengine clustered nozzle base flow physics were deduced from the analysis.

Numerical Modeling

The basic equations employed in this study to describe the base flowfield for a four-engine clustered nozzle are the three-dimensional, general-coordinate transport equations. These are equations of continuity, momentum, enthalpy, turbulent kinetic energy, and turbulent kinetic energy dissipation rate. A standard two-equation turbulence model is used to describe the turbulence.

Presented as Paper 93-1923 at the AIAA/SAE/ASME/ASEE 29th Joint Propulsion Conference and Exhibit, Monterey, CA, June 28–30, 1993; received Aug. 6, 1993; revision received Oct. 11, 1994; accepted for publication Nov. 22, 1994.

*Researcher, Computational Fluid Dynamics Branch. Member AIAA.

To solve the system of nonlinear partial differential equations (PDEs), it uses finite difference approximations to establish a system of linearized algebraic equations. An adaptive upwind scheme was employed to approximate the convective terms of the momentum, energy, and continuity equations; the scheme is based on second- and fourth-order central differencing with artificial dissipation. The dissipation terms are constructed such that a fourth-order central and fourth-order damping scheme is activated in smooth regions, and a second-order central and second-order damping scheme is used near shock waves. Viscous fluxes and source terms are discretized using second-order central difference approximation. A pressure-based predictor plus multicorrector solution method is employed so that flow over a wide speed range can be analyzed. The basic idea of this pressure-based method is to perform corrections for the pressure and velocity fields by solving a pressure correction equation so that velocity/pressure coupling is enforced, based on the continuity constraint at the end of each iteration. Details of the present numerical methodology are given in Ref. 2.

Computational Grid Generation

A typical layout of the computational grid is shown in Fig. 1. The four nozzles, which are conical with a cylindrical external shell, are equally spaced on a circular base.[1] Due to the symmetrical nature of the flowfield, only one-eighth of this layout is generated and used for the actual calculation. The two sides of the pie-shaped grid, as shown in Fig. 1, are the symmetry planes. Two grid zones were created. The first zone started at the base and included the nozzle and the plume region. The second zone (the outer shell) comprises the ambient air and a portion of the expanded plume.

Three algebraic grids were generated for the purpose of this report. The difference among these three grids can be visualized by taking a section from the nozzle symmetry plane that lies in between the nozzle centerline and model centerline, as shown in Fig. 1. Grid A has 34,030 points, whereas the grid density for grid B and C is 113,202 points. An ambient-to-total-pressure ratio, $P_a/P_0 = 39 \times 10^{-4}$, is chosen as the nozzle operating condition. The grid lines near the nozzle lip of grid C are slanted to match the Prandtl–Meyer expansion.

Boundary Conditions

To start the calculation, an axisymmetric nozzle flow solution at the prescribed nozzle condition was carried out in a separate manner. The converged flow solution was then mapped to a three-dimensional nozzle flowfield. The nozzle lip, nozzle outer wall, and the base were specified as no-slip wall boundaries. The exit planes of zones 1 and 2, the outer surface (shell) of zone 2, and the inlet plane of zone 2 (flush with the base shield plane) were specified as exit boundaries. In addition, a fixed (ambient) pressure was imposed on the inlet plane of zone 2 in order to obtain a unique solution for the corresponding altitude. Flow properties at the wall, symmetry plane, and exit boundary were extrapolated from those of the interior domain. A tangency condition was applied at the symmetry planes.

Results and Discussion

At this ambient pressure, which corresponds to an altitude of 91,800 ft, the four exhaust plumes have interacted and a reverse jet is formed. The reverse jet impinges on the center of the base and spreads out, forming a wall jet. This wall jet may be choked once the ambient pressure is lower than a critical limit. A comparison of the computed radial base pressure profiles with data is shown in Fig. 2. In general, the peak pressure occurred at the base center and the base pressure decreased as the radial distance from the center of heat shield increased.

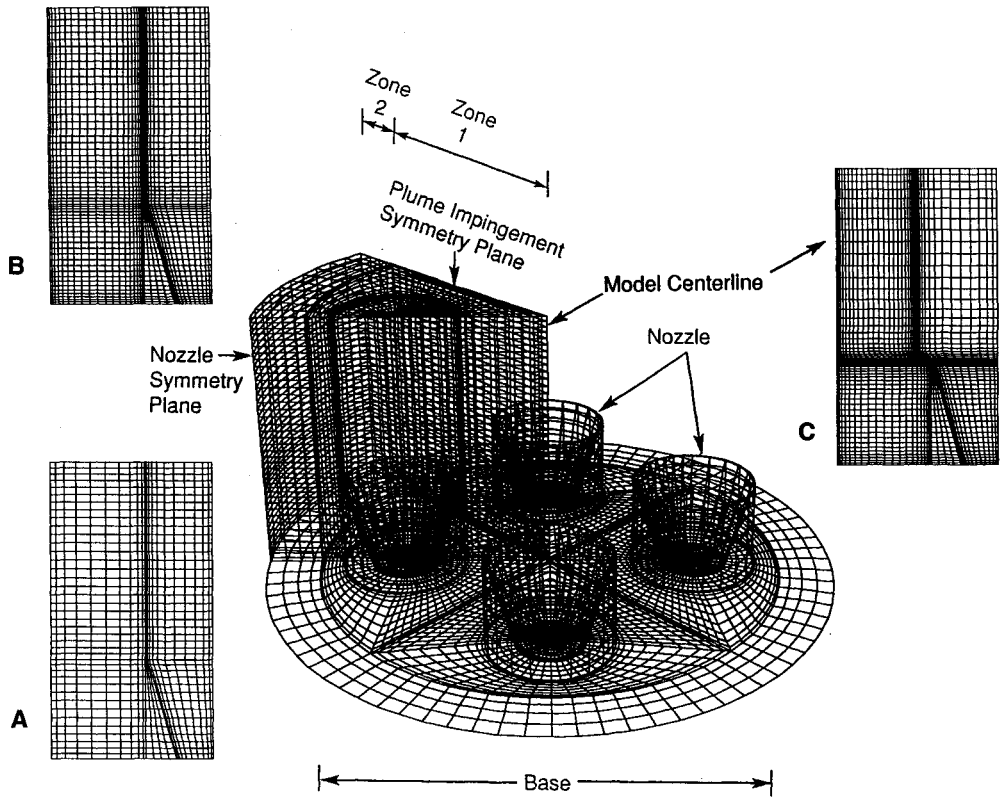

Fig. 1 Layout of a typical computational grid and slices of three different computational grids.

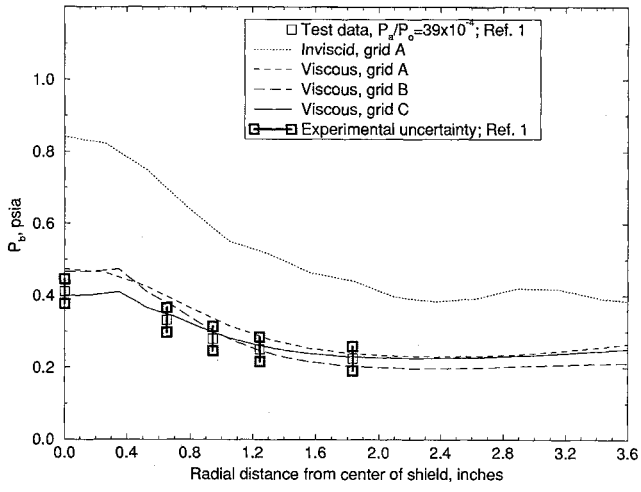

Fig. 2 Comparison of the radial base pressure distributions.

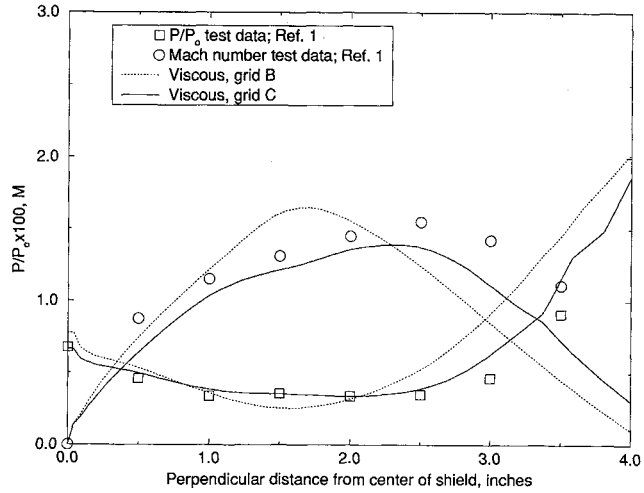

Fig. 3 Comparison of Mach number and static pressure variations along model centerline.

According to the inviscid multiengine clustered nozzle base flow theory proposed by Brewer,[1] the predominant amount of the reverse flow originates from the detached shock portion of the "inviscid plume impingement line," rather than the attached oblique shock recompression portion; hence, the shear layer type of analysis[5] for calculating the reverse flow is not applicable. The result of the inviscid flow solution on grid A indicates that the lateral velocity at the plume boundary had inviscid flow reversal, emanating from behind the detached shock portion of the plume impingement. Albeit the absolute magnitudes were overpredicted, the predicted trend is encouraging and confirms Brewer's theory on the origination of the reverse jet. However, the overpredictions indicate the inviscid flow theory requires improvement and the vast improvement in viscous solution on grid A demonstrated just that. That is, the viscous effect determines the strength of the reverse jet by resolving the shear layer and the level of the turbulence. The viscous grid B solution only improved slightly over that of viscous grid A, indicating the viscous resolution was not drastically improved with 3.3 times increase in grid density. Whereas the viscous solution of grid C matched the data very well, indicating the resolution of a Prandtl–Meyer expansion is probably more efficient than the sheer increase of the grid density.

Mach number and static pressure comparisons along model centerline, as shown in Fig. 3, assess the goodness of the model prediction for the strength of the reverse jet. The grid B prediction that overpredicted the central base pressure previously, also peaked too early in Mach number profile and bottomed too early in static pressure profile, indicating the acceleration of the reverse jet was too close to the base. The grid C solution, on the other hand, followed the data reasonably well. This result illustrated the importance of both Prandtl–Meyer expansion and viscous effect.

Conclusions

A three-dimensional, pressure-based CFD method is used to benchmark an experimental investigation of base flowfield for a four-engine clustered nozzle. The result of the analysis supported Brewer's inviscid flow theory[1] that the lateral flow emanating from behind the detached shock portion of the plume impingement dominated the creation of the reverse jet. It also goes one step further by showing that the strength of the reverse jet is determined by the viscous effect. In addition, computationally efficient base flowfield solution is obtained through Prandtl–Meyer expansion resolved grid treatment.

References

[1]Brewer, E. B., and Craven, C. E., "Experimental Investigation of Base Flow Field at High Altitude for a Four-Engine Clustered Nozzle Configuration," NASA TND-5164, Feb. 1969.

[2]Wang, T.-S., and Chen, Y.-S., "Unified Navier-Stokes Flowfield and Performance Analysis of Liquid Rocket Engines," *Journal of Propulsion and Power*, Vol. 9, No. 5, 1993, pp. 678–685.

[3]Korst, H. H., Chow, W. L., and Zumwalt, G. W., "Research on Transonic and Supersonic Flow of a Real Fluid at Abrupt Increases in Cross Section," ME Tech. Rept. 392-5, Univ. of Illinois, Urbana, IL, 1959.

Beam Waist/Focus Misalignment Error Estimates in Laser Doppler Anemometry

Clinton L. Dancey* and Jeffrey Hetmanski†
Virginia Polytechnic Institute and State University, Blacksburg, Virginia 24061

Introduction

IF the Gaussian beam waists in a path-compensated, dual-beam, fringe-mode laser Doppler anemometer (LDA) are coincident with the focus of the two beams (the point where the axes of the two beams cross), the interference fringe spacing at the focus d_{fm} is given by the familiar expression:

$$d_{fm} = \lambda/2 \sin(\kappa) \tag{1}$$

where λ is the laser wavelength and κ is the half-angle between the two transmission beams. If, on the other hand, the beam waists are misaligned, and therefore, not coincident with the focus, the fringe spacing d_f varies with position within the beam crossover region[1–5] and the nonuniformity of d_f within the LDA measurement volume results in mean fringe bias[5] and broadening errors.[1,3] Broadening error has been treated elsewhere, whereas mean fringe bias error, by comparison, has received relatively little attention. In this Note, the nature and magnitude of mean fringe bias error is considered. Specifically, it is shown that the "average" fringe spacing within the LDA measurement volume differs from that given by Eq. (1), even for "aligned" systems, and that the error is relatively insensitive to the degree of misalignment. It is also demonstrated by way of an illustration that the magnitude of the error is small for many practical LDA laser and optical arrangements.

Received Oct. 28, 1993; revision received Aug. 1, 1994; accepted for publication Sept. 20, 1994.

*Assistant Professor, Department of Mechanical Engineering. Member AIAA.

†Research Assistant, Department of Mechanical Engineering.

Background

Mean fringe bias error occurs since the computed fringe spacing based upon Eq. (1) and the measured angle κ only applies at the focus.[1] To illustrate, if it is assumed that the flow velocity is uniform and steady, the computed mean velocity, obtained from a large ensemble of individual measurements distributed over the measurement volume and utilizing the familiar equation

$$V = \nu d_{fm} \tag{2}$$

(where ν is the Doppler frequency and V is the velocity component perpendicular to the bisector of the two transmission beams), may be biased away from the true uniform steady value due to the unaccounted for variation of d_f within the measurement volume.

Alternatively, mean fringe bias may be described by defining an average or mean fringe spacing within the LDA measurement volume and comparing it to that given by Eq. (1). This is the approach taken in this Note. (Other forms of bias that may occur in LDA are neglected in this work.)

Mean Fringe Spacing

In a path-compensated dual-beam LDA d_f may be considered a function of position within the beam crossover region. That is $d_f(\xi)$, where ξ is a position variable. The mean fringe spacing $\langle d_f \rangle$ within the measurement volume is defined here by a conventional average:

$$\langle d_f \rangle = \left[\int_{\xi_m - L}^{\xi_m + L} d_f(\zeta)\, \mathrm{d}\zeta \right] \Big/ 2L \tag{3}$$

where ξ_m is the focus location and $2L$ is the length of the measurement volume.

In this Note, Hanson's theory of fringe divergence is used to derive an expression for $d_f(\xi)$ and Eq. (3) is employed to obtain $\langle d_f \rangle$. An equation for the fractional mean fringe bias

$$\frac{\langle d_f \rangle - d_{fm}}{d_{fm}} = \frac{\langle d_f \rangle}{d_{fm}} - 1 \tag{4}$$

is derived and the functional dependence of the bias on relevant LDA system parameters is made explicit. Finally, an illustrative example is presented.

Mean Fringe Bias Error

The front transmission lens and one of the two Gaussian beams of a dual beam LDA are shown in the sketch of Fig. 1. The focal distance f shown in the figure is the location (measured from the lens) where the centerline axes of the two laser beams cross. z_1 is the location of the beam waist (again measured from the lens). For the path-compensated case, and with some approximating assumptions, Hanson[1,2] showed that the variation in the Doppler frequency within the beam crossover region (which is not shown in the figure), is given by

$$\frac{\mathrm{d}\nu}{\nu\, \mathrm{d}\xi} = -\frac{1}{\xi[1 + (\pi\omega_1^2/\lambda\xi)^2]} \tag{5}$$

where ξ is the distance measured from the waist (see Fig. 1) along the dual-beam bisector to an arbitrary location within